Experimental study on shock wave control in high-enthalpy hypersonic flow by using SparkJet actuator☆

Wei Xie [a], Zhenbing Luo [a],[*], Yan Zhou [a],[**], Tianxiang Gao [a], Yun Wu [b], Qiu Wang [c]

[a] National University of Defense Technology, Changsha, 410073, China
[b] Air Force Engineering University, Xi'an, 710038, China
[c] Institute of Mechanics, Chinese Academy of Sciences, Beijing, 100097, China

ARTICLE INFO

ABSTRACT

SparkJet (SPJ) actuator was used to control shock and shock-on-shock interaction in high-enthalpy hypersonic flow with a total temperature of 4490 K and Mach number 6.9 for the first time. Aiming at the characteristics of rarefied gas in hypersonic flight environment, the control authority of SPJ actuator was improved by air supply method. The process of SPJ interacting with high-enthalpy hypersonic crossflow near a ramp was obtained by using high-speed schlieren camera. When pressurized cavity pressure was 133 kPa, ramp distance was 22 mm and ramp angle was 50, SPJ can eliminate 68.3 % of the whole ramp shock. Results of different experiment cases showed that, within a certain range, the control effect of SPJ on ramp shock improves with the increase of pressurized cavity pressure, ramp distance and the decrease of ramp angle. The elimination of shock by SPJ can be explained by the upward motion of the sonic line in the boundary layer due to the formation of SPJ shock, the thickening of boundary layer and the heating of local flow field. Except for the elimination of shock, the shock intersection point moves upstream and downstream corresponding to the strength changes of SPJ and SPJ shock. Accordingly, local high heat flow around the shock intersection point can be decreased. The control effect of SPJ on shock-on-shock interaction can be improved by properly increasing discharge energy.

1. Introduction

Hypersonic vehicle is one of the primary directions of aerospace development in the 21st century. However, there are still many key technical problems in the research of hypersonic vehicle. For example, in multiple tests of HTV-2 hypersonic vehicle in 2010–2011, due to shock/shock interference and shock/boundary layer interference of hypersonic flow, high heat flow was generated around the vehicle; and then thermal protection system of the vehicle was burned abnormally, resulting in the failure of the test finally. In 2011, the second test of the X-51A hypersonic vehicle also failed because the inlet did not start due to shock/boundary layer interference. In addition, the drag brought by shock, which takes up more than 50 % in the total drag of hypersonic vehicle in the case of high atmospheric density, has a great impact on the improvement of hypersonic vehicle performance. Therefore, it is of great significance to explore effective flow control methods to overcome or alleviate these serious shock-related problems in hypersonic flow [1–3].

Plasma-based actuators [4–6], with advantages of fast response, wide bandwidth, and no moving components, have become one of the hotspots in active flow control and have broad application prospects in the field of high-speed flow control [7–9]. SparkJet (SPJ) actuator [10], also called "plasma synthetic jet actuator, pulsed plasma jet", is a new type of plasma-based actuator with great potential for super-sonic/hypersonic flow control. It is composed of an insulated cavity with a small exit and a pair of electrodes. A high voltage is applied between the two electrodes for the breakdown of cavity gas, and the gas in the confined cavity is rapidly heated and pressurized. In the meantime, high-temperature, high-speed SPJ and a strong compression wave (also called as "precursor shock" or "blast wave") [11,12] are formed at the exit. After SPJ is ejected, SPJ actuator will automatically aspirate air in the environment due to the low pressure in the cavity. At this point, one operation cycle of SPJ actuator is completed in only a few hundred microseconds. Actually, SPJ actuator is a fusion of jet actuator (such as synthetic jet and continuous jets) and plasma actuator [13,14]. It has

significant advantages, including both high jet speed, strong penetration ability of jet actuator and fast response speed, no moving parts or fluid supply device, and wide excitation frequency band of plasma actuator.

Proposed by Grossman in 2003 [10], plenty of studies have proved the control authority of SPJ actuator [15–17], meanwhile, there are also a variety of studies focused on its structure optimization, efficiency improvement and parameter characterization [18–22]. In recent years, SPJ actuator has gradually been used to solve shock-related problems in supersonic flow. Wang et al. [23] studied how the transverse SPJ interacted with the shock induced by the 24° ramp in a supersonic flow with Mach number 2. The schlieren images showed that the shock was significantly modified by SPJ with an upstream motion and a reduced angle. Another research by Zhou et al. [24] showed that shock induced by a 25° compression ramp in Mach 2 flow was significantly weakened by SPJ and the near-wall part of the shock was eliminated. In the experiment conducted by Huang et al. [25], a shock-on-shock interaction occurred when the SPJ shock intersected with the shock induced by a 20° compression ramp in Mach 2 flow and the interaction gradually changed from a regular one to an irregular one with a Mach stem in the middle of the two shocks. In addition, SPJ was also verified to be effective in the control of supersonic separation, separation shock, and shock/boundary layer interaction [26–29].

However, the effectiveness of SPJ under the conditions of high enthalpy, hypersonic and rarefied flow has yet to be experimentally verified. The high-enthalpy hypersonic incoming flow is closer to the real flight state of hypersonic vehicle than the conventional hypersonic incoming flow. The difference between the two mainly lies in "high-temperature gas effect (real gas effect)", which exists widely in the high-enthalpy hypersonic flow. To promote the application of SPJ actuator in hypersonic vehicles, an experiment was conducted to investigate the control of shock and shock-on-shock interaction by using SPJ actuator in high-enthalpy hypersonic flow in the present study. This is the first time to apply SPJ actuator in high-enthalpy hypersonic flow. Air supply, with the purpose of simulating the secondary flow ejected from the high-pressure area of vehicle [30,31], was adopted to pressurize SPJ actuator. Electrical properties and interaction process with ramp-induced shock and shock-on-shock interaction of SPJ actuator with air supply were attained and discussed.

2. Experimental setup

The experiment was carried out in JF-X shock tunnel of the Institute of mechanics, Chinese Academy of Sciences. As shown in Fig. 1, the shock tunnel, about 20 m long, composites of driver section, driven section, nozzle, test section and vacuum. The lengths of driver section and driven section are 6.44 m and 6.86 m, respectively, and the diameters of both are 126 mm. The length of nozzle is 1.5 m and the diameter of nozzle exit is 0.5 m. The length and diameter of test section are respectively 1 m and 0.8 m. The test section is equipped with horizontal and vertical optical quartz glass windows for flow visualization. The basic flow parameters in the test section are shown in Table 1.

The schematic diagrams of test model and discharge circuit are shown in Fig. 2. The SPJ actuator is embedded into the central plate, which is installed in the test section of shock tunnel. The cavity of SPJ actuator is a cuboid, with length, width, and height of 12 mm, 9 mm and 8 mm. A round exit with a diameter of 4 mm is in the center of SPJ

Table 1
Parameters of incoming flow in the test section.

Parameters	Value	Unit
Mach number (Ma)	6.9	–
Velocity	3439	m/s
Total temperature	4490	K
Static temperature	688	K
Total pressure	6.4	MPa
Static pressure	1458	Pa
Duration	5	ms

actuator, i.e., SPJ exit. Two tungsten electrodes (anode and cathode) with a diameter of 1 mm are installed in the cavity for gas breakdown and the electrode gap is 4 mm. A ramp, with angle of 25° or 50° and width of 15 mm, is installed 22 mm downstream of SPJ exit and the distance (ramp distance) is adjustable. The NS-3 pressure sensor, which consists of two cylinders, with dimensions of 5 mm in diameter and 5 mm in height, and 10 mm in diameter and 18 mm in height, respectively, is used to measure the pressure in the cavity. The NS-3 pressure sensor has an uncertainty of 0.4 kPa, which is calibrated by the manufacturer. A cylinder inlet with a diameter of 4 mm is used to supply high-pressure air. A switching power supply, a solenoid valve and a solid-state relay are used to control the on-off of air supply system. The power supply system mainly consists of a high-voltage pulsed capacitive power supply (model KD-1, designed by the High Voltage Laboratory of Xi 'an Jiaotong University in China), which can provide voltage slightly higher than 10 kV. The high-voltage pulsed capacitive power supply mainly includes a DC power supply (500V, 1000 W), an IGBT (Insulated Gate Bipolar Transistor), a high-voltage pulse transformer (1:20). In addition, a capacitor of 0.32 μF is arranged to store energy in the circuit, accelerating the discharge of SPJ actuator. The discharge voltage and current between anode and cathode was measured using a P6015A high-voltage probe and a Pearson current coil respectively. For all experiment cases, voltage and current were measured simultaneously, recorded, and stored by DPO4104 oscilloscope. The voltage and current measurement have uncertainty of 0.4 kV and 0.1 kA, respectively, which is gained from both the measurement error and ten groups of measurement data under the same conditions. The DG535 four-channel digital delay/pulse signal generator is used as the trigger device.

The schlieren system is arranged in transmission mode, with a point light source, the fastcam-SA4 high-speed digital camera, two convex lenses and a knife edge, etc, as shown in Fig. 3. The light source was spherical short-arc-xenon lamp (XQ type, 500 W). Two convex lenses with focal length of 2.5 m were used to collimate the light through the test section. A Photron FASTCAM SA-Z camera with an AF NIKKOR 80–200 mm f/2.8D ED lens was used to capture schlieren images. The exposure time was set to 1.2 μs to provide an instantaneous snapshot of the flow. The spatial resolution of the camera was 0.2 mm/pixel, the minimal resolution of the image was 0.5 pixel. Therefore, the precursor shock and PSJ location measured from the schlieren images had an uncertainty of ±0.1 mm. In order to ensure the resolution of schlieren images, the frame rates were set to 40,000 fps, 70,000 fps and 75,000 fps in this experiment, consequently, the time interval between two images (Δt) is 25 μs, 14 μs and 13.3 μs respectively.
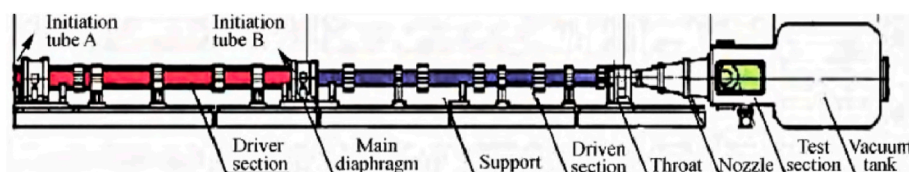
Fig. 1. Schematic diagram of JF-X shock tunnel.

(a) Schematic diagram of central plate

(b) Section view of SPJ actuator
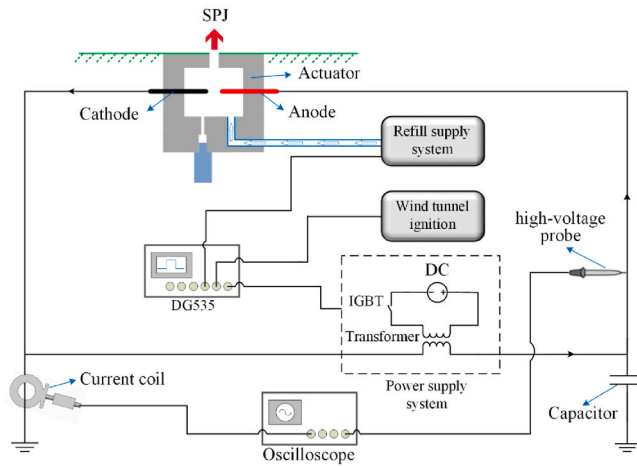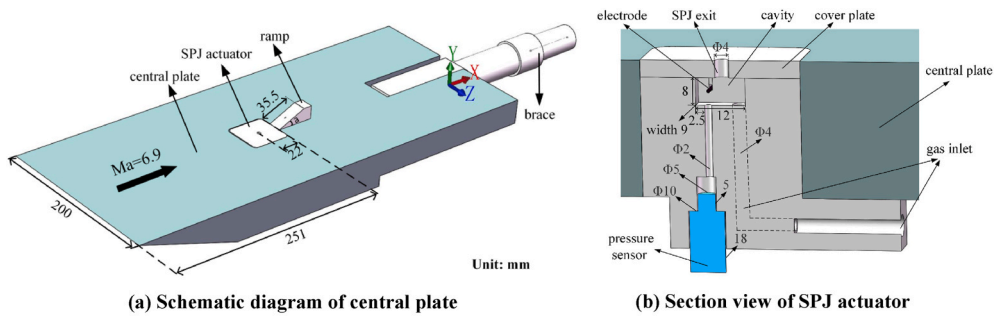
(c) Schematic diagram of discharge circuit

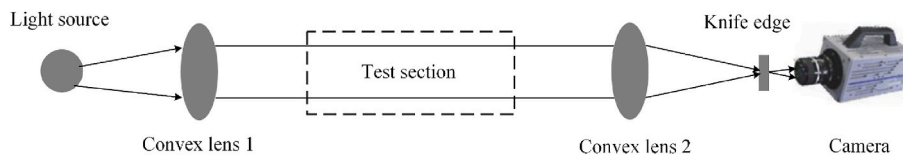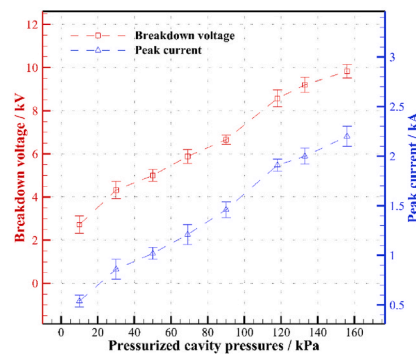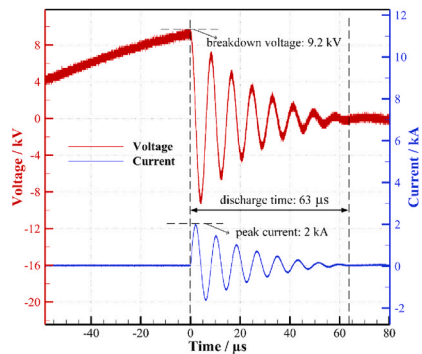**Fig. 2.** Schematic diagram of test model and discharge circuit.

Fig. 3. Schematic diagram of schlieren setup in the experiment.

(a) Discharge voltage and current waveform with

pressurized cavity pressure of 133 kPa

(b) Breakdown voltage and peak current with different

pressurized cavity pressures

Fig. 4. Discharge characteristics of SPJ actuator.

3. Experimental results and discussion

3.1. Discharge and flow field characteristics of SPJ actuator with air supply

Fig. 4 (a) represents the discharge voltage and current waveform of SPJ actuator when the pressurized cavity pressure (the pressure of SPJ actuator cavity with air supply) is 133 kPa. The results show that the breakdown voltage and the peak current are approximately 9.2 kV and 2 kA respectively. According to Paschen's law of gas discharge, when the electrode gap is fixed at 4 mm, the increase of cavity pressure has a great influence on the discharge of SPJ actuator. It can be seen from Fig. 4 (b) that breakdown voltage and peak current gradually increase with pressurized cavity pressure. The error bars are gained from 10 repeated tests.

The flow field evolution of SPJ actuator with pressurized cavity pressure of 133 kPa in quiescent air is shown in Fig. 5. After discharge, SPJ and precursor shock are quickly ejected out of the cavity. The precursor shock in front of SPJ is more prominent with pressurized cavity pressure of 133 kPa, compared with SPJ without air supply [11,12,18]. This phenomenon is caused by the existence of the steady jet. Based on the position difference of jet front in the schlieren image sequence, the jet front velocity can be calculated [18,32,33]. As mentioned above, the spatial resolution of the camera is 0.2 mm/pixel, and the frame interval is about 13.3 μs (75,000 fps). Therefore, the estimated error of velocity calculated is about 15 m/s. The estimated jet front velocity is shown in Fig. 6. The velocity of SPJ with air supply (over 800 m/s) was significantly increased compared to that without air supply (less than 500 m/s) [11,12,18]. The data used is averaged through five similar schlieren results under the same condition.
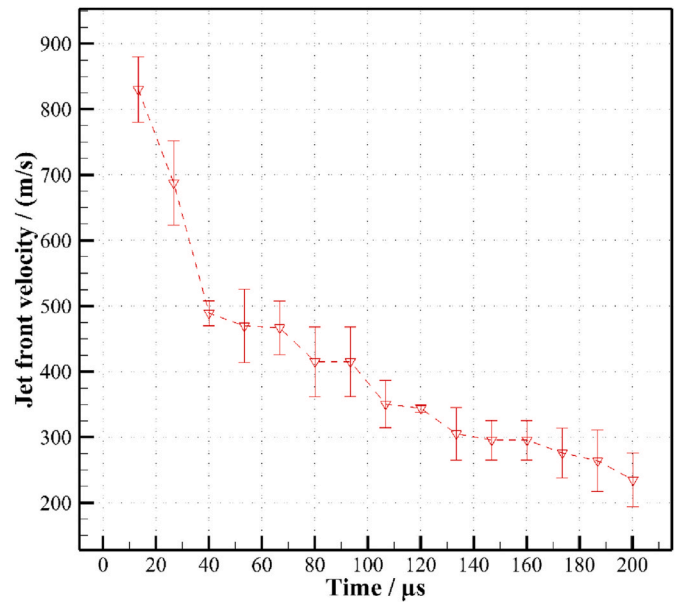

Fig. 6. Jet front velocity of SPJ (with pressurized cavity pressure of 133 kPa) in quiescent air.

3.2. Interaction between SPJ and high-enthalpy hypersonic crossflow near a ramp

Fig. 7 shows the interaction process between SPJ and high-enthalpy hypersonic crossflow near the ramp during a single discharge using the schlieren images. This experimental case is set with pressurized cavity pressure of 133 kPa, ramp angle of 50° and ramp distance of 22 mm. The discharge energy ($E = 1/2CU^2$) is about 13.5 J and the discharge
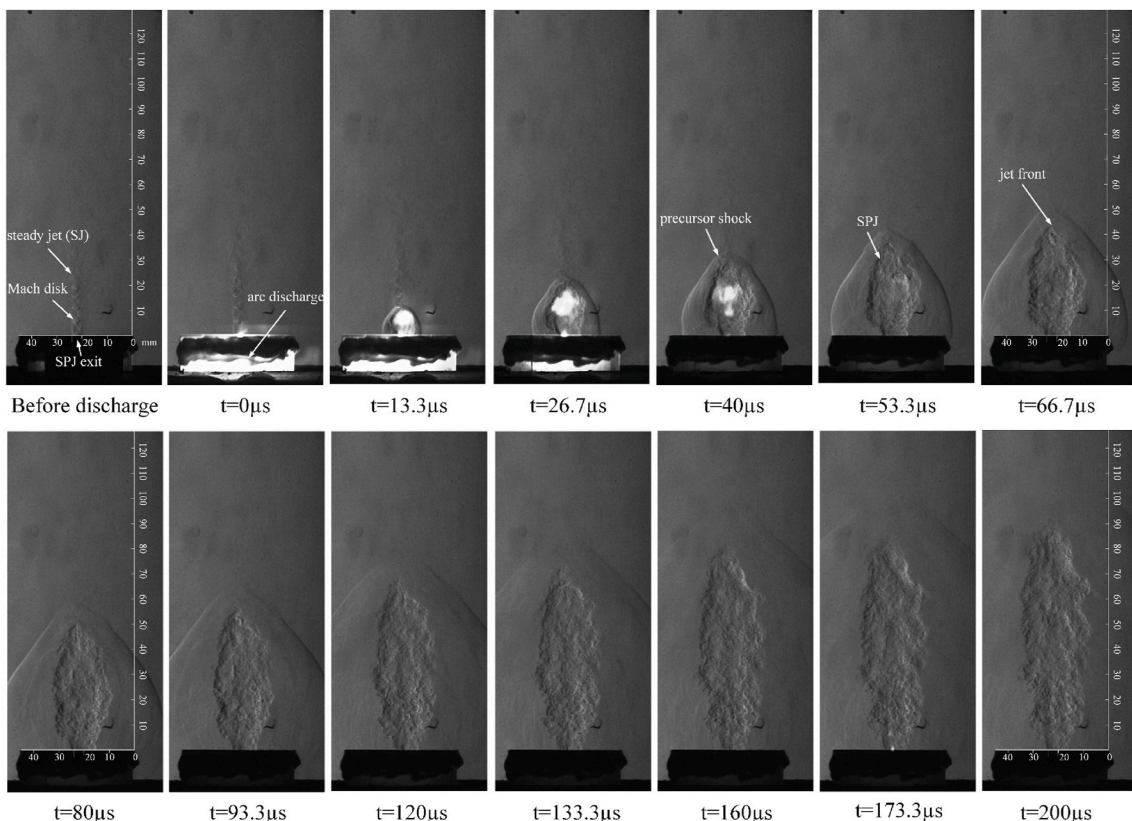

Fig. 5. Schlieren image sequence of SPJ (with pressurized cavity pressure of 133 kPa) in quiescent air.
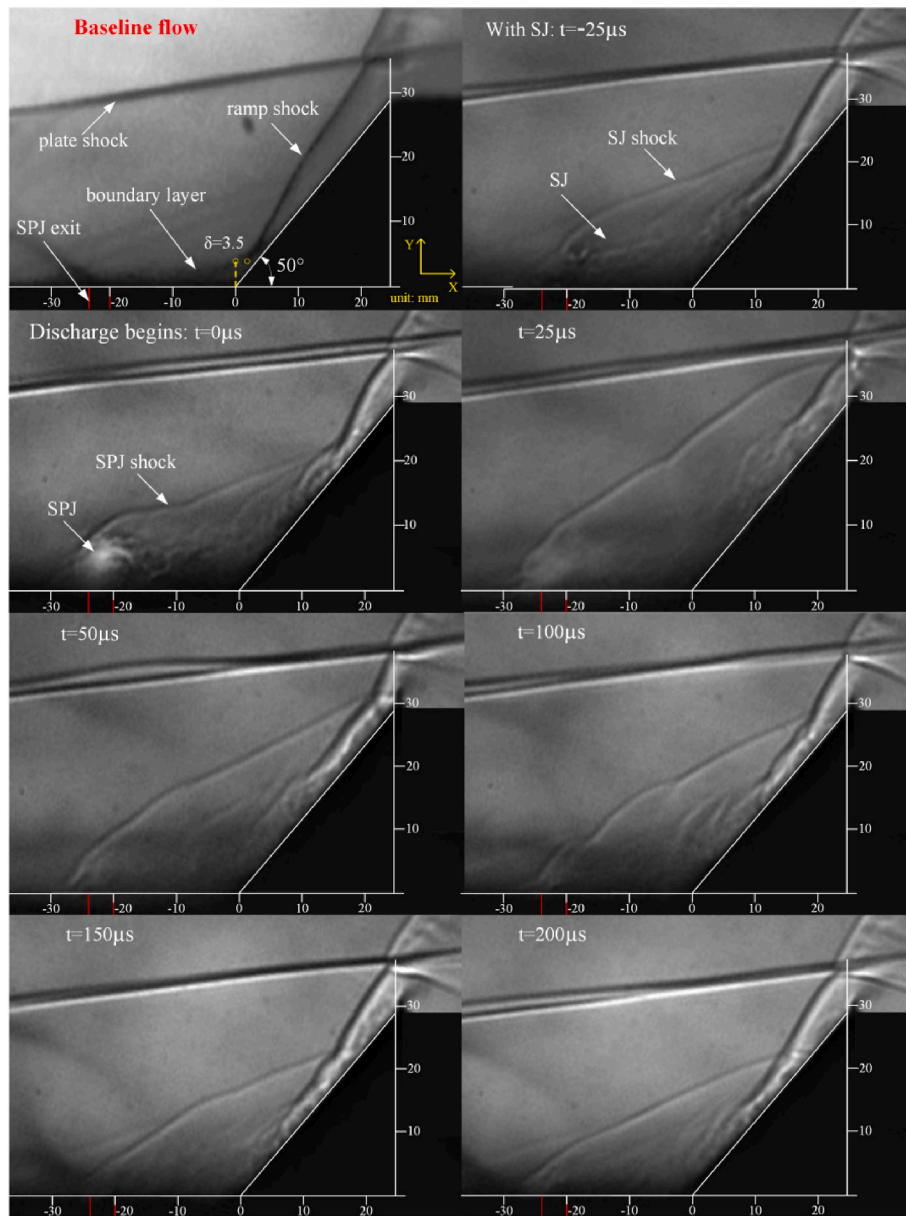
Fig. 7. Schlieren image sequence of SPJ (with pressurized cavity pressure of 133 kPa) interacting with high-enthalpy hypersonic crossflow near a ramp.

duration is about 63 μs, as shown in Fig. 4 (a). For the convenience of expression, the jet formed at the SPJ exit due to air supply is called "steady jet (SJ)". The shock generated by the interaction between SJ and hypersonic flow is called "steady jet shock (SJ shock)". The shock generated by the interaction between SPJ and hypersonic flow is called "SPJ shock" and the shock induced by the ramp is called "ramp shock".

Fig. 7 first shows the baseline flow without control. A strong ramp shock is formed due to the 50° ramp. In addition, there is a strong oblique shock called "plate shock" on the top of the schlieren image, which is generated by the leading edge of the central plate. As the distance between the SPJ actuator and the plate shock is far enough, the plate shock has little effect. So "ramp shock" in the latter description refers to the ramp shock below the plate shock (with length of about 44.5 mm). The thickness of boundary layer (δ) at X = 0 mm is approximately 3.5 mm, which also equals to the Y-coordinate of the root of ramp shock. δ is used for the dimensionless of length. t = −25 μs corresponds to the schlieren image with SJ, that is, with the control of SJ. With pressurized cavity pressure of 133 kPa, SJ continuously ejects from SPJ exit; and a SJ shock is formed upstream. It can be observed that a

small proportion of ramp shock has been eliminated by SJ and SJ shock. When t = 0 μs, it corresponds to the time when discharge begins and from t = 0 μs–25 μs, the coverage of SPJ and SPJ shock gradually increases. At t = 25 μs, the coverage of SPJ shock has covered nearly the whole ramp shock and a large part of ramp shock is invisible in the image (that is, has been eliminated). After t = 25 μs, the strength of SPJ shock and SPJ gradually decreases, corresponding to which the ramp shock gradually reforms. At t = 200 μs, the flow field basically recovers the state before discharge. It can be concluded that, in this case, the work cycle of SPJ is approximately 200 μs.

Based on the schlieren images, schematic of flow features and sonic lines of SJ (SPJ)/hypersonic crossflow interaction are shown in Fig. 8 for qualitative analysis. The positions of the sonic lines in Fig. 8 only represents the schematic position before and after the control, not the actual position obtained from the schlieren images. Point A and B are respectively denoted as the root of ramp shock and the intersection point of SJ (SPJ) shock with ramp shock. Point A also represents the intersection point of the sonic line in the boundary layer and the ramp shock. The elimination of ramp shock and the coverage of SJ/SPJ shock of
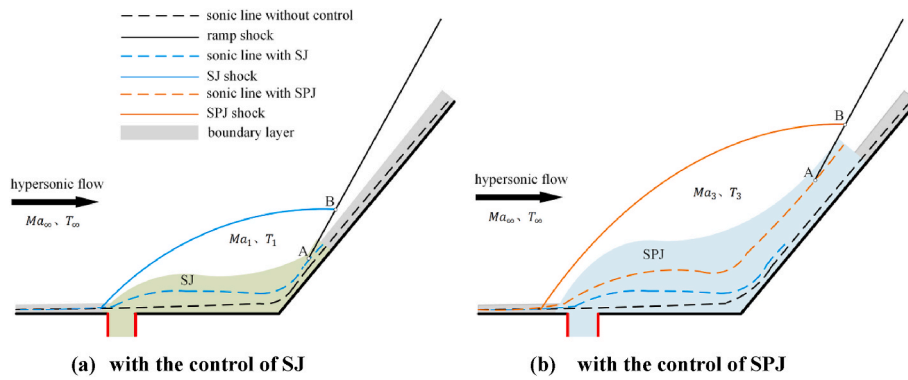
(a) with the control of SJ   **(b) with the control of SPJ**

Fig. 8. Schematic of flow features and sonic lines with the control of SJ and SPJ.

schlieren image sequence in Fig. 7 can be concluded from the Y-coordinate changes of point A and B, as is shown in Fig. 9. As previously mentioned, Y-coordinate of point A in the baseline flow are 3.5 mm, which is approximate to the thickness of boundary layer (δ) at X = 0 mm. Y-coordinate of point A increases to 3.3δ with the control of SJ and Y-coordinate of point B is 6.5δ with the formation of SJ shock at t = −25 μs. Y-coordinate of point A and B continue to change with the formation of SPJ and SPJ shock. For the limit of camera frame rate, the phenomenon between two images is unknown. So, the analysis is conducted with the limited images. At t = 25 μs, Y-coordinate of point A and B reach their maximum of 7.3δ and 10.3δ respectively. The angle of ramp shock is approximately 57° and the maximum length of ramp shock eliminated by SPJ and SPJ shock is approximately 8.7δ in this experimental case, accounting for 68.3 % of the whole ramp shock (about 12.7δ). After t = 25 μs, Y-coordinate of point A and B gradually decrease but point A decreases faster than B. Y-coordinate of point A remains 3.4δ to 4δ with a slight variation after about t = 75 μs. While Y-coordinate of point B keeps decreasing until about t = 200 μs, when the Y-coordinate value is approximately equal to the one before discharge.

The phenomenon that part of the ramp shock is eliminated can be explained based on schlieren images of Fig. 7 and schematic of flow features in Fig. 8. On the one hand, SJ shock and SPJ shock decrease the Mach number and increase temperature of the incoming flow, ($Ma_1 <$
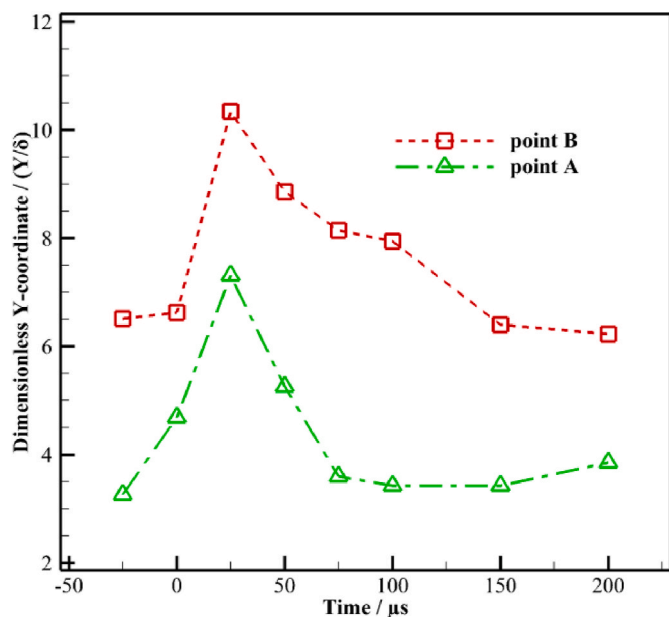
Ma_∞, $T_1 > T_\infty$, $Ma_3 < Ma_\infty$, $T_3 > T_\infty$). As a result, ramp shock in the coverage of SJ shock and SPJ shock is weakened due to the decrease of Mach number. On the other hand, SJ and SPJ can be regarded as new thicker boundary layers, which lead to the sonic line in the boundary layer moving upward to some extent. In addition, as a kind of high-temperature jet, the peak temperature measured of SPJ by using digital speckle tomography (DST) is about 1600 K 1.85 mm downstream the SPJ exit [34]. Once the wall and the boundary layer are heated, the local Mach number will decrease rapidly and correspondingly the sonic line in the boundary layer will move up further rapidly [35]. To conclude, elimination of ramp shock by SPJ lies in the upward motion of the sonic line in the boundary layer due to the formation of SPJ shock, the thickening of the boundary layer and the heating of the local flow field.

3.3. Effect of different parameters on the interaction between SPJ and ramp shock

To study the effect of different parameters on the interaction between SPJ and ramp shock, four cases are set for comparison. As shown in Table 2, case1 is the case demonstrated in detail in Fig. 7, compared to which pressurized cavity pressure, ramp distance and ramp angle are changed, respectively in case2, case3 and case4.

Fig. 10 manifests schlieren images of SPJ interacting with high-enthalpy hypersonic crossflow near a ramp in four experimental cases. Each schlieren image represents the best control effect of SPJ on the ramp shock of each case. Based on the quantitative analysis in 3.2, Table 2 also lists the maximum Y-coordinates of point A and point B and the proportion of eliminated ramp shock under four circumstances. The proportion of eliminated ramp shock is defined by the ratio of the length of the eliminated ramp shock and the length of the whole ramp shock (about 12.7δ). The eliminated ramp shock can be calculated by the ratio of Maximum Y-coordinate of point A and sin (57°), of which 57° is the angle of ramp shock. For case1 and case2, SPJ and SPJ shock with pressurized cavity pressure of 133 kPa in case1 are stronger than that of 69 kPa in case2 because the discharge energy is much larger. As a result, the proportion of eliminated ramp shock is 68.3 % in case1 and 45.3 % in case2. At the same time, the time corresponding to the optimal control effect (about t = 100 μs) in case2 is slightly delayed compared to that in

Fig. 9. Changes of dimensionless Y-coordinate of point A and B in schlieren images of Fig. 4

Table 2
Experimental cases set and comparison of control effect.

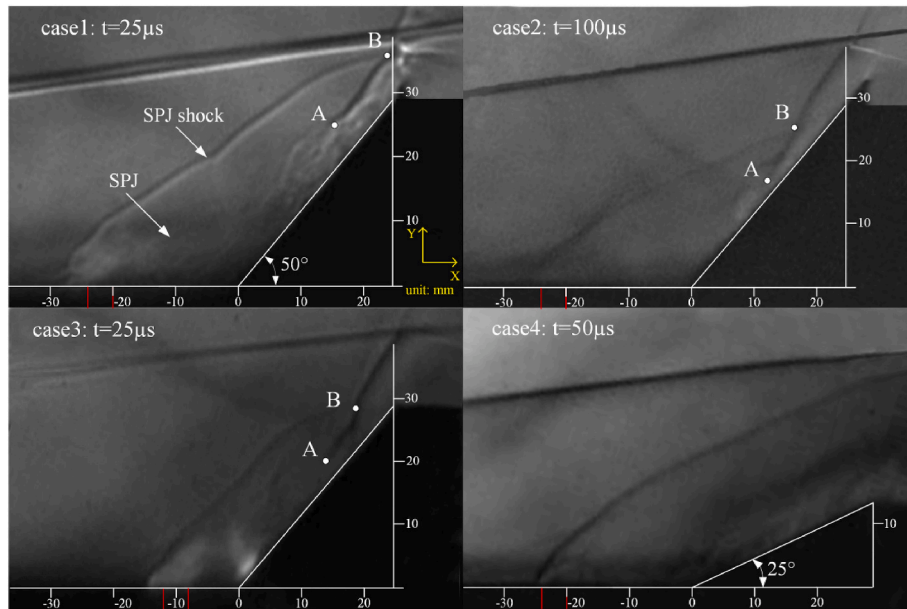| Parameters	case1	case2	case3	case4
Pressurized cavity pressure/kPa	133	69	133	133
Discharge energy/J	13.5	5.8	13.5	13.5
Ramp distance/mm	22	22	10	22
Ramp angle/ °	50	50	50	25
(Maximum Y-coordinate of point A)/δ	7.3	4.9	5.8	–
(Maximum Y-coordinate of point B)/δ	10.3	7	8.1	–
Proportion of eliminated ramp shock/-	68.3 %	45.3 %	53.9 %	100 %

Fig. 10. Schlieren images of SPJ with different parameters interacting with high-enthalpy hypersonic crossflow near a ramp.

case1 (about t = 25 μs). When the ramp distance decreased from 22 mm to 10 mm in case3, the proportion of eliminated ramp shock is 53.9 %, compared to 68.3 % in case1. In case3, when the SPJ exit is closer to the ramp, the SPJ cannot be fully developed before interacting with the ramp shock, which affects its control effect to a certain extent. When the ramp angle decreased from 50° to 25° in case4, ramp shock induced by the ramp is much weaker and the proportion of eliminated ramp shock is 100 %, that is, the ramp shock is eliminated by SPJ shock and SPJ, completely.

3.4. Control of shock-on-shock interaction by SPJ

The interaction between two shocks of the same type in hypersonic flow, especially the interaction at the intersection of shocks, will cause extremely high local heat flow and seriously restrict the development of hypersonic vehicle. This type of shock-on-shock interaction, also known as an Edney type VI interaction [36], exists extensively in hypersonic flow. For example, the interaction between plate shock and ramp shock, SPJ shock and ramp shock have already been shown in Figs. 7 and 10. In this section, our discussion will concentrate on the control of type VI shock-on-shock interaction by using SPJ actuator.

Fig. 11 is the schematic diagram of the test model in this section. Angle of ramp1 and ramp2 are 30° and 45° respectively and both ramp2
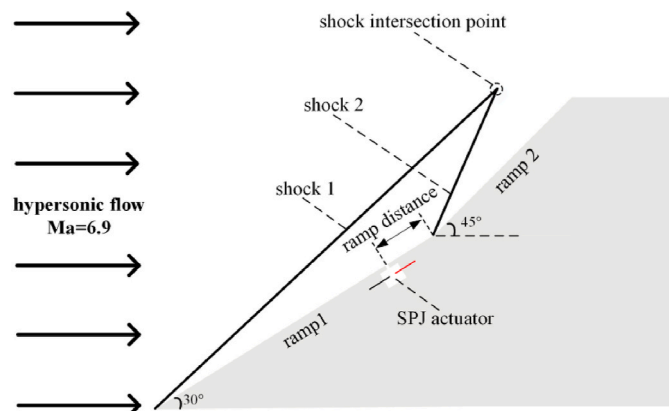
and SPJ actuator are located on ramp1. In hypersonic flow, the two ramps will generate two oblique shock waves and there will be a shock intersection point at some place, which may give rise to strong local heating around. The free-stream conditions are the same as described previously.

As shown in Table 3, three cases are set in the experiment to study the control authority of single-pulsed SPJ on shock-on-shock intersection. The discharge was also set with repetition rate of 1 Hz. By comparing case5 and case6, it can be concluded that the increase of capacitance has little effect on the breakdown voltage and peak current. From comparison of case7 with case5, it can be seen that breakdown voltage and peak current increase significantly with pressurized cavity pressure of 84 kPa. In addition, the discharge energy increases with the increase of both the capacitance and the pressurized cavity pressure and the discharge duration increases with the increase of discharge energy, as shown in Table 3.

Fig. 12 shows the interaction process between SPJ and shock-on-shock interaction of case6 by using schlieren images. The camera frame rate is 70,000 fps, so the time interval between the two images is about 14 μs. There are two oblique shock waves (shock1 and shock2) and a shock intersection point (point C) before discharge (t = −14 μs). t = 0 μs corresponds to the time when discharge begins. As stated previously, analysis is done from the limited images for the limit of camera frame rate. From t = 0 μs–28 μs, coverage of SPJ and SPJ shock gradually increases. The shock intersection point C is eliminated by SPJ, completely, while the new shock intersection point D formed by shock1 and SPJ shock is formed upstream and gradually moves upstream until t = 28 μs. X = 0 corresponds to X-coordinate of point C, so X-coordinate of point D reflects the distance between point C and D. The location of point D can represent the coverage of SPJ shock and reflect the control

Fig. 11. Schematic of test model for control of shock-on-shock interaction.

Table 3
Experimental cases set and comparison of electrical properties.

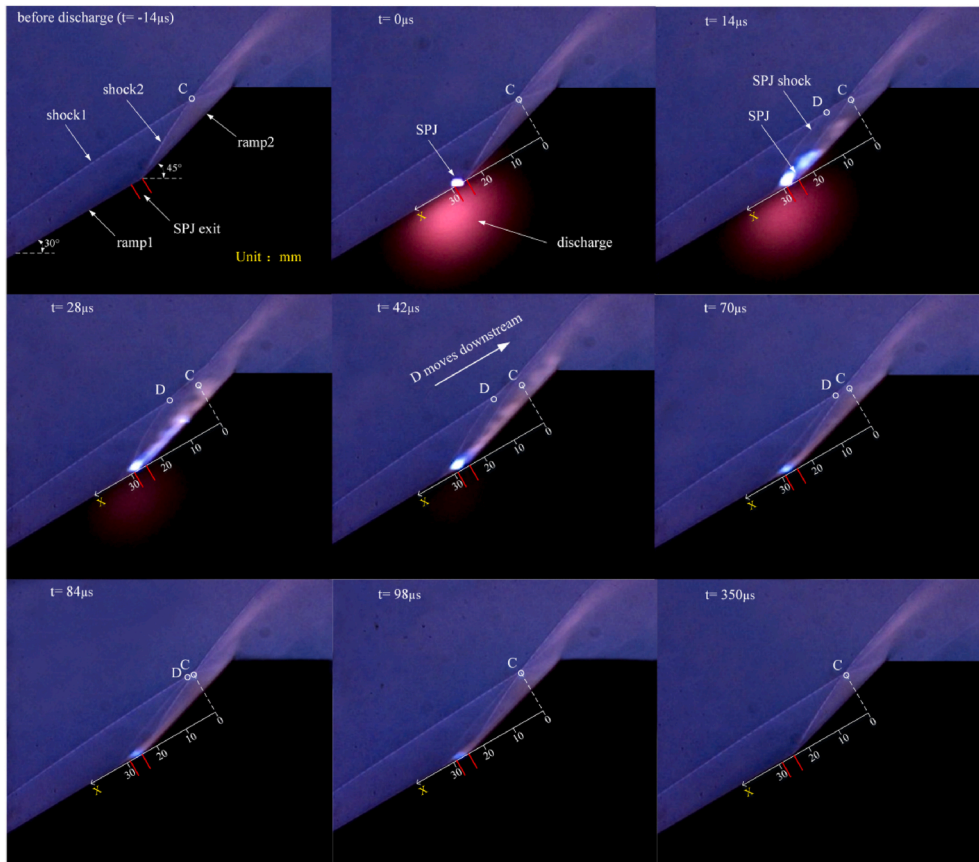| Parameter	Case5	Case6	Case7
Capacitance/μF	0.64	1.6	0.64
Ramp distance/mm	2	2	10
Pressurized cavity pressure/kPa	18	18	84
Breakdown voltage/kV	3.6	3.32	8.3
Peak current/kA	1.2	1.7	2.52
Discharge energy/J	4.1	8.8	22
Discharge duration/μs	53	68	90

Fig. 12. Schlieren image sequence of SPJ interacting with shock-on-shock interaction of case6.

effect of SPJ and SPJ shock to some extent. At t = 28 μs, coverage of SPJ shock has covered nearly the whole shock2 and part of shock1. From t = 28 μs to t = 98 μs, SPJ and SPJ shock gradually weaken and shock2 gradually recover. At the same time, the new shock intersection point D keeps moving downstream. After about 98 μs, point D and point C coincide and remain steady. However, there are still weak SPJ and SPJ shock formed at the exit. The flow field completely recovers to the state before discharge at about 350 μs. So with the control of SPJ, except for eliminating the shock, which is the same as that described in section 3.2, high local heat flow can be decreased due to the motion of shock intersection point.

Fig. 13 shows the schlieren images at t = 28 μs in three cases. At t = 28 μs, X-coordinate of point D in three cases all reach their maximum, which also reflects the best control effect of SPJ on shock-on-shock interaction. Some useful information can be attained via comparing the three images. On the one hand, the coverage of SPJ and SPJ shock gradually increases from case5, case6 to case7, as can be inferred from the increase of the X-coordinate of point D (7 mm, 9.5 mm and 28.2

mm). On the other hand, in case6 and case7, it is evident that shock2 and shock intersection point C is eliminated completely by SPJ and SPJ shock; while there is still part of shock2 in case5, which has not been eliminated. The above analysis shows that the increase of discharge capacitance in case6 and increase of pressurized cavity pressure in case7 help to improve the control authority of SPJ on shock-on-shock interaction.

The detailed changes of X-coordinate of point D with time in three experimental cases are shown in Fig. 14. For case5 and case6, X-coordinate of point D reaches the maximum value of 7 mm and 9.5 mm respectively at t = 28 μs. After that, X-coordinate of point D gradually decreases due to the weakening of SPJ and SPJ shock. After t = 98 μs for case5 and t = 84 μs for case6, point D and C coincide and X-coordinate of point D remains stable at 0 mm. For case7, due to the increase of ramp distance (10 mm) and the existence of SJ and SJ shock, X-coordinate of point D at t = 0 μs is approximately 15 mm. Also, at t = 28 μs, the maximum value of X-coordinate of point D is 28.2 mm. Notably, much weaker than the first one as they are, there are several more times of SPJ
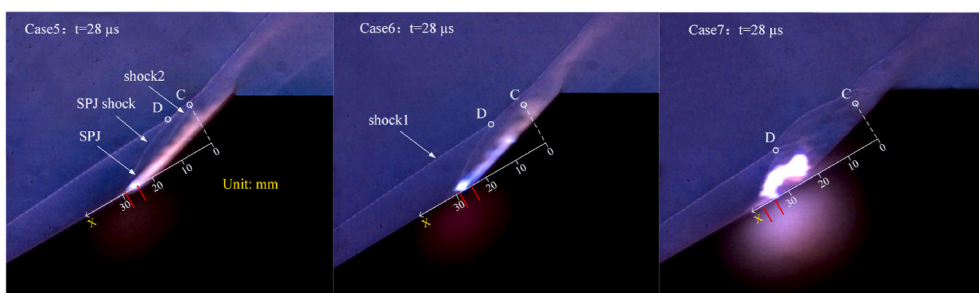

Fig. 13. Comparison of control effect of SPJ on shock-on-shock interaction in three cases.
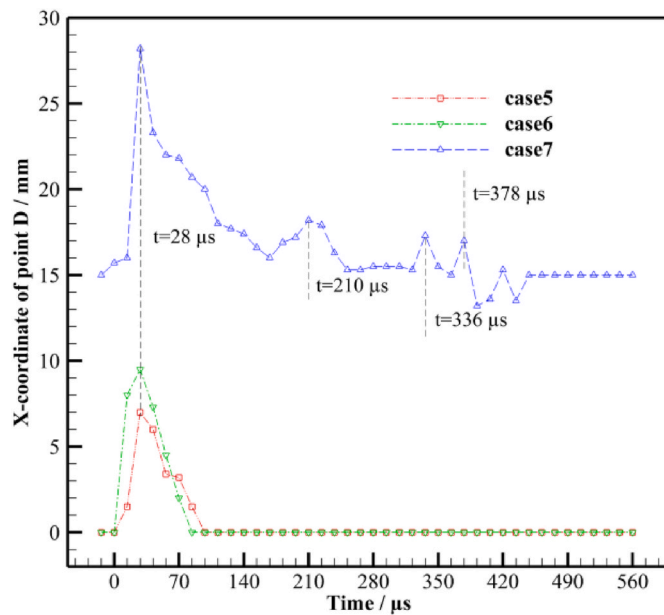
Fig. 14. Changes of X-coordinate of point D with time in three experimental cases.

ejection in case7. As shown in Fig. 14 at t = 210 μs, t = 336 μs and t = 378 μs, there is a small peak value in each of the time corresponding to SPJ ejection for the second, third and fourth time. After t = 378 μs, X-coordinate of point D gradually remains stable at about 15 mm with small oscillations.

4. Conclusions

In the present study, control of shock and shock-on-shock interaction in high-enthalpy hypersonic flow by using SPJ actuator is investigated experimentally. This is the first application of SPJ actuator to a high-enthalpy hypersonic flow.

(1) Air supply was used to improve the performance of SPJ actuator. The breakdown voltage and the peak current of SPJ actuator increase with the increase of pressurized cavity pressure in a certain range. SPJ can eliminate 68.3 % of the ramp shock when the pressurized cavity pressure is 133 kPa, ramp distance is 22 mm and ramp angle is 50°. The control effect of SPJ on ramp shock can be improved by increasing pressurized cavity pressure, ramp distance, and reducing ramp angle within limits.

(2) The SPJ ejected into the hypersonic crossflow can be regarded as a new thicker boundary layer. The elimination of shock by SPJ can be attributed to the upward motion of the sonic line in the boundary layer due to the formation of SPJ shock, thickening of the boundary layer and heating of the local flow field.

(3) SPJ can eliminate both shock and shock intersection point in high-enthalpy hypersonic flow. When the original shock intersection point is eliminated, the upstream will form a new shock intersection point, corresponding to the strength change of SPJ and SPJ shock, moving upstream and downstream. With the control of SPJ, high local heat flow around the shock intersection point can be decreased. Increase of discharge capacitance and pressurized cavity pressure help to improve the control authority of SPJ on shock-on-shock interaction.

Further work may focus on accurately simulating how SPJ interacts with shock as limited flow details can be obtained from experimental methods under the influence of electromagnetic interference. In addition, the control of more complex shock-on-shock interaction and shock

wave/boundary layer interaction by using SPJ actuator may also be a promising direction.

Data availability

The data that support the findings of this study are available from the corresponding author upon reasonable request.

Declaration of competing interest

The authors declare that they have no known competing financial interests or personal relationships that could have appeared to influence the work reported in this paper.

References

[1] W. Huang, H. Wu, Y.G. Yang, et al., Recent advances in the shock wave/boundary layer interaction and its control in internal and external flows, Acta Astronaut. 174 (2020) 103–122.

[2] K. Ma, Y. Li, L. Zhu, et al., Spike root oblique jet effect on drag and heat load reduction performance for hypersonic vehicles, Acta Astronaut. 177 (2020) 588–603.

[3] J. Huang, W.X. Yao, Active flow control by a novel combinational active thermal protection for hypersonic vehicles, Acta Astronaut. 170 (2020) 320–330.

[4] W.Z. Wang, M. Jia, R. Feng, et al., Experimental investigation on the gliding arc plasma supported combustion in the scramjet combustor, Acta Astronaut. 177 (2020) 133–141.

[5] J.J. Wang, K.S. Choi, L.H. Feng, et al., Recent developments in DBD plasma flow control, Prog. Aero. Sci. 62 (2013) 52–78.

[6] E. Pescini, D.S. Martinez, M.G. Degiorgi, et al., Optimization of micro single dielectric barrier discharge plasma actuator models based on experimental velocity and body force fields, Acta Astronaut. 137 (2017), 522-522.

[7] S.J. Ju, Z.X. Sun, G.W. Yang, et al., Parametric study on drag reduction with the combination of the upstream energy deposition and the opposing jet configuration in supersonic flows[J], Acta Astronaut. 171 (2020) 300–310.

[8] M.Z. Dong, J. Liao, G. Choubey, et al., Influence of the secondary flow control on the transverse gaseous injection flow field properties in a supersonic flow, Acta Astronaut. 165 (2019) 150–157.

[9] M.X. Tang, Y. Wu, S.G. Guo, et al., Effect of the streamwise pulsed arc discharge array on shock wave/boundary layer interaction control, Phys. Fluids 32 (7) (2020), 076104.

[10] K.R. Grossman, B.Z. Cybyk, D.M. VanWie, Sparkjet Actuators for Flow Control, AIAA, Reston, 2003. Report No.: AIAA-2003-57.

[11] T.M. Reedy, N.V. Kale, J.C. Dutton, et al., Experimental characterization of a pulsed plasma jet, AIAA J. 51 (8) (2013) 2027–2031.

[12] A. Belinger, P. Hardy, N. Gherardi, et al., Influence of the spark discharge size on a plasma synthetic jet actuator, IEEE Trans. Plasma Sci. 39 (11) (2011) 2334–2335.

[13] S. Traficante, M.G. De Giorgi, A. Ficarella, Flow separation control on a compressor-stator cascade using plasma actuators and synthetic and continuous jets, J. Aero. Eng. 29 (3) (2016), 04015056.

[14] M.G. De Giorgi, A. Ficarella, F.M. Elisa Pescini, Micro DBD plasma actuators for flow separation control on a low pressure turbine at high altitude flight operating conditions of aircraft engines, Appl. Therm. Eng. 114 (2017) 511–522.

[15] V. Narayanaswamy, L.L. Raja, N.T. Clemens, Characterization of a high-frequency pulsed-plasma jet actuator for supersonic flow control, AIAA J. 48 (2) (2010) 297–305.

[16] K.V. Anderson, D.D. Knight, Plasma jet for flight control, AIAA J. 50 (9) (2012) 1855–1872.

[17] R.B. Liu, Z.G. Niu, M.M. Wang, et al., Aerodynamic control of NACA 0021 airfoil model with spark discharge plasma synthetic jets, Sci. China Technol. Sci. 58 (11) (2015) 1949–1955.

[18] L. Wang, Z.X. Xia, Z.B. Luo, et al., Three-electrode plasma synthetic jet actuator for high-speed flow control, AIAA J. 52 (4) (2014) 879–882.

[19] Y. Zhou, Z.X. Xia, Z.B. Luo, et al., A novel ram-air plasma synthetic jet actuator for near space high-speed flow control, Acta Astronaut. 133 (2017) 92–102.

[20] M. Golbabaei-Asl, D. Knight, Novel technique to determine sparkjet efficiency, AIAA J. 53 (2) (2015) 501–882.

[21] Y. Zhou, Z.X. Xia, Z.B. Luo, et al., Experimental characteristics of a two-electrode plasma synthetic jet actuator array in serial, Chin. J. Aeronaut. 31 (12) (2018) 2234–2247.

[22] H.H. Zong, M. Kotsonis, Formation, evolution and scaling of plasma synthetic jets, J. Fluid Mech. 837 (2018) 147–181.

[23] H.Y. Wang, J. Li, D. Jin, et al., Effect of a transverse plasma jet on a shock wave induced by a ramp, Chin. J. Aeronaut. 30 (6) (2017) 1854–1865.

[24] Y. Zhou, Z.X. Xia, Z.B. Luo, et al., Effect of three-electrode plasma synthetic jet actuator on shock wave control, Sci. China Technol. Sci. 60 (1) (2017) 150–156.

[25] H.X. Huang, H.J. Tan, S. Sun, et al., Transient interaction between plasma jet and supersonic compression ramp flow, Phys. Fluids 30 (2018), 041703.

[26] V. Narayanaswamy, J. Shin, N.T. Clemens, et al., Investigation of Plasma-Generated Jets for Supersonic Flow Control, AIAA, Reston, 2008. Report No.: AIAA-2008-285.

[27] B.R. Greene, N.T. Clemens, P. Magari, Control of mean separation in shock boundary layer interaction using pulsed plasma jets, Shock Waves 25 (2015) 495–505.

[28] G. Yang, Y.F. Yao, J. Fang, et al., Large-eddy simulation of shock-wave/turbulent boundary layer interaction with and without sparkjet control, Chin. J. Aeronaut. 29 (3) (2016) 617–629.

[29] Zhang ZB, Zhang XN, Wu Y, et al. Experimental research on the shock wave control based on one power supply driven plasma synthetic jet actuator array. Acta Astronaut., AA-D-20-00006.

[30] Y. Zhou, Z.X. Xia, Z.B. Luo, et al., Characterization of three-electrode sparkjet actuator for hypersonic flow control, AIAA J. 57 (2) (2019) 879–885.

[31] Qiang Liu, Z.B. Luo, X. Deng, et al., Vortical structures and density fluctuations analysis of supersonic forward-facing step controlled by self-sustaining dual synthetic jets, Acta Mech. Sin. (2020) (Article in press).

[32] Zong Zhi-Bo Zhang, et al., Influence of capacitor energy on performance of a three-electrode plasma synthetic jet actuator, Sens. Actuators, A (2015).

[33] H.H. Zong, M. Kotsonis, Effect of slotted exit orifice on performance of plasma synthetic jet actuator, Exp. Fluid 58 (3) (2017) 1–17.

[34] S.J. Haack, H.B. Land, B. Cybyk, et al., Characterization of a High-Speed Flow Control Actuator Using Digital Speckle Tomography and PIV, AIAA, Reston, 2008. Report No.: AIAA-2008-3759.

[35] B. Holger, K.H. John, Shock Wave-Boundary-Layer Interactions, Cambridge University, 2011.

[36] B. Edney, Anomalous Heat Transfer and Pressure Distributions on Blunt Bodies at Hypersonic Speeds in the Presence of an Impinging Shock, Aeronautical Research Institute of Sweden, 1968. FFA report 115.